

# Duke University

Active Microwave Imaging System for Breast Cancer  
Screening: RF MEMS Switching Matrix System Design

by

Tawanda Chaunzwa

*Department of Electrical and Computer Engineering*

Research Advisor: Dr. Ybarra



<b>I. Introduction</b>	3
<b>II. RF MEMS Switching Matrix System</b>	4
1. Motivation	4
2. Background	4
2.1 Agilent Advanced Design System (ADS)	4
2.2 Interconnection Lines (Transmission Lines)	5
2.3 RF Microelectromechanical System (MEMS) Switches	8
3 Transmission Line Characterization	11
3.1 Coplanar Waveguide	11
3.2 Microstrip	14
4. Switching System Design	17
4.1 Multiplexer Design	17
4.2 Switching System Characterization	18
<b>III. Development of numerical breast phantoms</b>	20
1. Motivation	20
2. Breast Anatomy	20
2.1 Adipose Tissue	21
2.2 Glandular Tissue	21
2.3 Skin and Connective Tissue	21
3. Electrical Properties of Breast Tissue	21
3.1 Normal Breast Tissue	22
3.2 Malignant Tissue	23
3.3 The relationship of permittivity and conductivity	24
3.4 Cole-Cole Models	25
<b>IV. Remaining Work and Conclusions</b>	25
<b>Acknowledgements</b>	26
<b>References</b>	27

# I. Introduction

Breast cancer is one of the most prominent types of cancer among women. It ranks second among cancer deaths in women after lung cancer [1]. Detection of this type of cancer at an early stage increases the likelihood of successful treatment hence it is the best solution short of a complete cure [2]. Currently, X-ray mammography is the most effective method for the screening of breast cancer. However, X-ray mammography has important limitations. First, conventional mammography is less sensitive in women with radiographically dense breast tissue [1]. This is mainly because x-ray imaging depends on the differences in the density of breast tissues for contrast. Second, mammography suffers from a high false-positive rate. A report by the U.S. Institute of Medicine (IOM) in 2001 revealed that roughly 10 percent of mammograms contained images with possible tumors, but less than one in ten of those were actually diagnosed as malignancies [2]. In addition, the false negative rate of mammography is also not insignificant, and there are possible health risks associated with x-ray's ionizing radiation.

These limitations provide considerable motivation for the development of alternative and/or complementary forms of breast imaging. In recent years, there has been a great deal of interest in imaging modalities for detecting and characterizing breast tissue that utilize nonionizing energy in the microwave frequency range [3]. The most important reason for the attraction to this frequency range for this application is that it balances the trade-off between spatial resolution for imaging and penetration depth [3]. The emergence of active microwave imaging is motivated by a number of previously published data that shows a substantial contrast in the electrical properties (permittivity and conductivity) of normal and malignant breast tissues at microwave frequencies [3]. For normal and malignant human tissues of the same histological type, the largest difference in the electrical properties has been observed in the mammary gland relative to colon, kidney, liver, lung and muscle [2]. Another rationale for pursuing active microwave imaging is that the breast presents a small volume that is easily accessible, making it a more manageable site for effective imaging than larger anatomical areas [2].

In this paper I present the work from two separate projects that I worked on as part of the Active Microwave Research group at Duke. In Section II, the work on the design and development of RF MEMS switching matrix system is presented. Unfortunately, we did not receive the switches in time to build the switching matrix system; hence the work that is presented is mostly the simulations results that were obtained using the measured data of scattering parameters of MEMS switches that was provided to us by RadantMEMS. I also worked on a separate project to develop numerical breast phantoms. This work is presented in Section III. The results from the literature study of the electrical properties of different breast tissues are presented in the section. The knowledge of these properties is important for the development of anatomically realistic numerical breast phantoms that model structural complexities, tissue heterogeneity, and dispersive dielectric properties [4].

## **II. RF MEMS Switching Matrix System**

### **1. Motivation**

The switching system that is currently used for active microwave breast screening at Duke University is made up of transistor-based electronic switches that perform poorly at high frequencies, have poor channel isolation and are very lossy. The objective of this project is to design and develop an alternative switching system using microelectromechanical system (MEMS) based RF switches. RF MEMS switches provide ultra-low losses, high isolation, long life cycle (100 billion cycles), high switching speed and linearity [5]. In addition, these switches have significant size, power consumption and cost advantages of high volume wafer fabricated solid state switches [5]. Development of this new switching system would greatly improve the sensitivity of the imaging system and the spatial sampling density.

### **2. Background**

#### **2.1 Agilent Advanced Design System (ADS)**

The work on the development of the RF MEMS switching matrix system was divided into two main parts: the design and characterization of the transmission lines (the interconnection lines) and the characterization of the system's subnetworks (receive and transmit networks). Agilent Advanced Design System (ADS), an industry standard microwave engineering computer-aided-design (CAD) program, was used for these design processes. This program has a single, integrated design environment which provides system and circuit simulators, along with schematic capture, layout and verification capability- hence supports every step of the design process and increases the design productivity by eliminating the stops and starts associated with changing the design tools in mid-cycle. In addition, the program has a full set of simulation technologies which allows the full characterization and optimization of RF/microwave design processes [6].

We used two methods to design/simulate in ADS: schematic (equation-based) and Momentum (Methods-of-Moments). The schematic simulator uses equations to obtain the S-parameters and other electrical properties of components under test. Momentum, a 3-D planar electromagnetic (EM) simulator used for passive circuit analysis, solves the Maxwell's equation for the design. Momentum is more accurate and efficient for circuit design/simulation. In addition, Momentum is capable of accepting arbitrary design geometries (including multi-layer structures) and accurately simulates complex EM effects including coupling and parasitic [7]. It is particularly efficient for analyzing transmission lines - microstrip and coplanar waveguides.

## 2.2 Interconnection Lines (Transmission Lines)

### 2.2.1 Coplanar Waveguide

A coplanar waveguide with the center conductor separated from a pair of ground planes, all on the same plane, atop a dielectric medium is shown in Figure 1. The physical dimensions of a CPW include the conductor width ( $W$ ), the conductor thickness ( $t$ ), the slot width/gap ( $G$ ), the substrate height ( $h$ ), and the relative dielectric constant ( $\epsilon_r$ ).

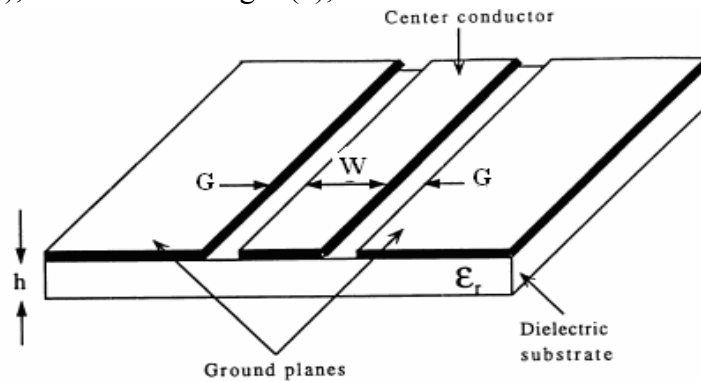


Figure 1: The generic view of a coplanar waveguide [8]

If a ground plane is provided on the opposite side of the dielectric substrate then the transmission line is called a grounded coplanar waveguide. In addition, if the ground plane at the bottom of the dielectric substrate is connected to the ground planes atop the substrate through via holes then the transmission line is called a conductor backed coplanar waveguide [9]. The use of via holes lower electromagnetic interference (EMI) radiation of conductor backed coplanar waveguides compared to common waveguides. However, compared to the usual coplanar waveguides the values of the impedance can be changed as a result of the presence of the via holes [9]. The top and cross views of the conductor backed coplanar waveguide are shown in Figure 2.

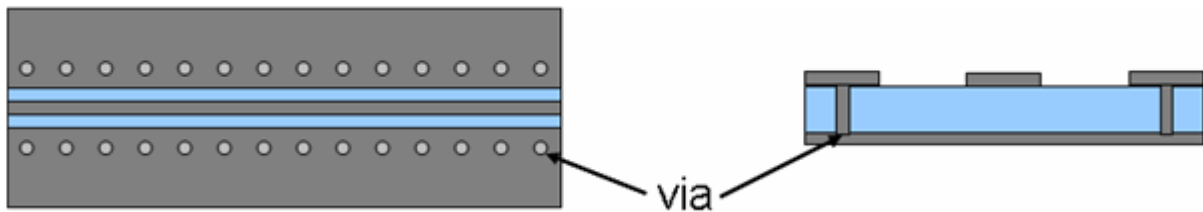


Figure 2: Top view (left) and cross section of the conductor backed coplanar waveguide [9]

In Figure 2 the center conductor and background planes are shown in grey and the substrate is shown in blue. The vias are shown connecting the ground planes on top of the substrate to the ground plane on the bottom side.

CPW has two dominant modes of propagation: quasi-TEM mode known as the odd mode or coplanar mode, and non quasi-TEM mode known as the even mode or the coupled slotline mode [11]. In the coplanar mode the fields in the two slots are  $180^\circ$  out of phase while in the coupled slotline mode the fields are in phase, Figure 3.

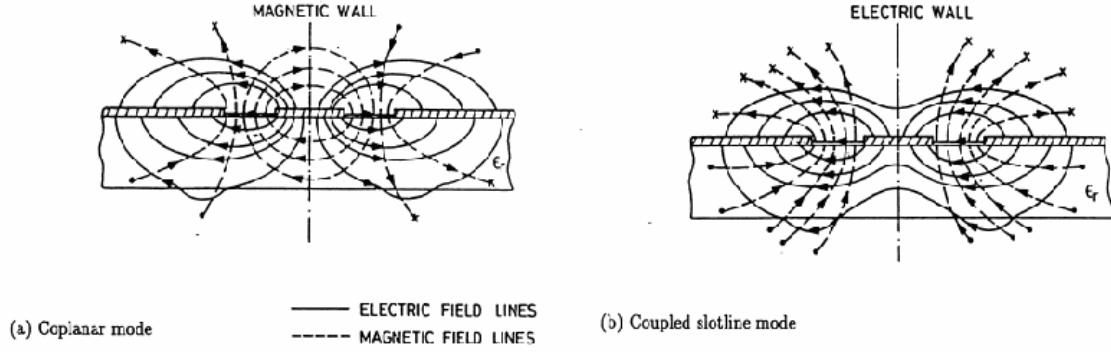


Figure 3: The coplanar and coupled slotline mode field configurations [10]

In CPW microwave circuits, the coplanar mode is the most desired due to its low radiation properties. The excitation of the unwanted slotline mode can be avoided by either maintaining the symmetry of the structure or using air-bridges (or bond-wires) to connect the ground planes of the CPW [10].

The coplanar waveguides designed and simulated for this project are grounded coplanar waveguides. The characteristic impedance of CPW is related to its physical dimensions as follows.

$$\eta = \sqrt{\frac{\mu_o}{\epsilon}}$$

$$Z_o = \begin{cases} \eta \frac{\pi/4}{\ln\left(\frac{4W}{G} + 2\right)}, & \frac{W}{G} \geq 3 \\ \frac{\eta}{2\pi} \ln\left(\frac{8G}{W} + 4\right), & \frac{W}{G} \leq 3 \end{cases}$$

where  $\eta$  is the electromagnetic impedance (intrinsic impedance) in a region with no conductivity [11].

The characteristic impedance and phase velocity of CPW are more depend on the aspect ratio,  $G/W$ , than on the substrate height ( $h$ ) [10]. The substrate height ( $h$ ) plays a less important role in CPW than in microstrip lines because in CPW the fields are concentrated in the slots [10].

### 2.2.2 Microstrip

A microstrip transmission line consists of a conducting strip separated from the ground plane by a dielectric medium (substrate), Figure 4. The physical dimensions of the transmission line include the substrate thickness ( $d$ ), the strip conductor width ( $W$ ), the strip conductor thickness ( $t$ ), and the dielectric constant of the substrate ( $\epsilon_r$ ) [12].

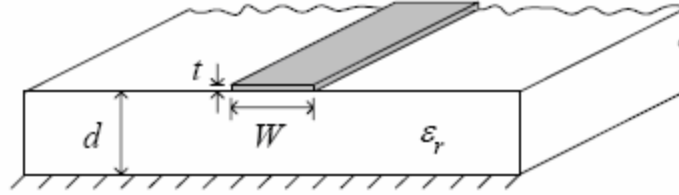


Figure 4: Microstrip transmission line [12]

For a microstrip there is more than one dielectric in which the electromagnetic (EM) fields are located; part of the fields from the strip conductor exist in air, thus the wave is traveling in an inhomogeneous medium, Figure 5.

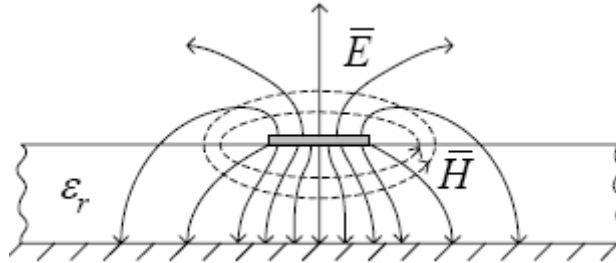


Figure 5: Distribution of the EM on a microstrip [12]

Consequently, the effective dielectric constant ( $\epsilon_{r,e}$ ) is less than the dielectric constant of the substrate. And because of the inhomogeneous medium there is no purely TEM wave on the microstrip but a quasi-TEM [13]. Another consequence of an inhomogeneous medium is that the microstrip has a dispersive behavior. This is because the effective dielectric constant gradually climbs to the dielectric constant of the substrate with increasing frequency and as a result the phase velocity gradually decreases [12].

$$v_p = \frac{c_o}{\sqrt{\epsilon_r}}$$

The numerical technique, methods of moments, used by ADS Momentum produce very accurate numerical solutions to the equations derived from Maxwell's equations and incorporate the exact cross-sectional geometry and materials of the microstrip [12].

The characteristic impedance of the quasi-TEM mode of the microstrip can be approximated by the following equations [12],

$$Z_o = \begin{cases} \left( \frac{60}{\sqrt{\epsilon_{r,e}}} \ln \left( \frac{8d}{W} + \frac{W}{4d} \right) \right) & \frac{W}{d} \leq 1 \\ \frac{120\pi}{\sqrt{\epsilon_{r,e}} \left[ \frac{W}{d} + 1.393 + 0.667 \ln \left( \frac{W}{d} + 1.444 \right) \right]} & \frac{W}{d} \geq 1 \end{cases}$$

The effective relative dielectric constant, phase velocity and phase constant, respectively, for the quasi-TEM mode are:

$$\begin{aligned}\epsilon_{r,e} &= \frac{\epsilon_r + 1}{2} + \frac{\epsilon_r - 1}{2} \frac{1}{\sqrt{1 + 12d/W}} \\ v_p &= \frac{c_o}{\sqrt{\epsilon_{r,e}}} \\ \beta &= k_o \sqrt{\epsilon_{r,e}}\end{aligned}\quad [12]$$

In microstrip lines, the level of parasitic radiation is strongly affected by the dielectric substrate thickness ( $d$ ) [10]. This complicates high frequency design because of the little flexibility in choosing appropriate substrate structures. And since mechanical considerations put a lower limit on the physical thickness of substrates used in circuit designs, it is difficult to avoid excessive loss in microstrip lines where the fields penetrate the whole substrate when operating above 100 GHz [10].

A comparison of microstrip and coplanar waveguide lines is shown in Table 1. The characterization of these two types of lines using ADS will be discussed shortly.

**Table 1: Comparison of microstrip and coplanar waveguide lines**

Characteristic	Microstrip	Waveguide
Line losses	High	Low
Unloaded Q	Low	High
Power capability	Low	High
Isolation between neighboring circuits	Poor	Very good
Bandwidth	Large	Small
Miniaturization	Excellent	Poor
Volume and weight	Small	Large
Realization of passive circuits	Very easy	Easy
Integration		
With chip devices	Very good	Poor
With ferrites	Good	Good
With lumped elements	Very good	Poor

### 2.3 RF Microelectromechanical System (MEMS) Switches

RF MEMS switches are electrostatically actuated cantilever beams connected in a three terminal configuration- source, drain and gate- similar to that of a field effect transistor.



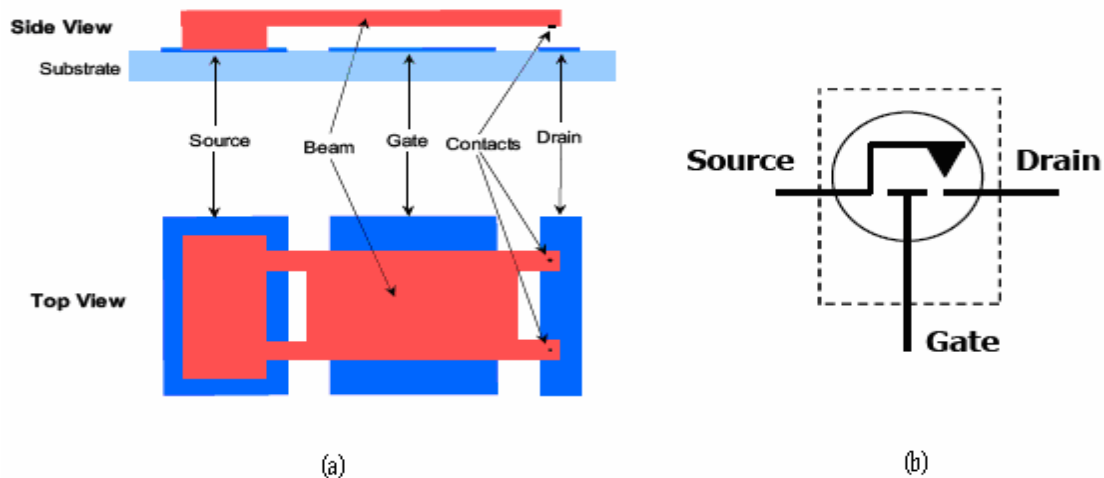


**Figure 6: (a) Side and top views of a SPST RF MEMS switch, (b) Functional block diagram of a SPST MEMS switch. Source: [www.radantmems.com](http://www.radantmems.com)**

When a bias DC voltage is applied between the gate and the source an electrostatic force results that causes the beam to deflect toward the substrate; the contacts on the beam touch the drain and complete the circuit between the source and the drain when the bias voltage exceeds the threshold voltage. When the bias voltage is removed, the beam acts as a spring, generating sufficient restoring force to open the connection between source and drain, thus breaking the circuit. The gate to source bias voltage is insensitive to polarity.

Compared to competing technologies such as transistor-based electronic switches that were previously used in the Duke imaging system, MEMS switches provide lower loss, higher isolation, longer life cycle (over 100 billion cycles), high switching speed, and higher linearity. In addition, they have significant size, power consumption and cost advantages of high volume wafer fabricated solid state switches. With lower insertion loss, distortion and power consumption, the device is ideally suited for the application of transmitter/receiver switching.

A sample circuit board with one SPDT switch and SMA connectors is shown in Figure 7. This device operates well from DC to about 40GHz, and since this range easily includes our operating frequency, 2.7 GHz, it suits our purpose.

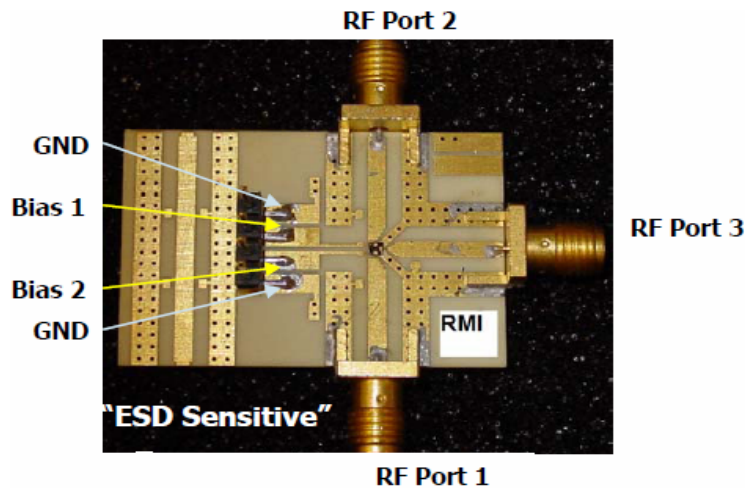


Figure 7: Circuit board with a SPDT switch. Source: [www.radantmems.com](http://www.radantmems.com)

The typical RF performance of this device is shown in below.

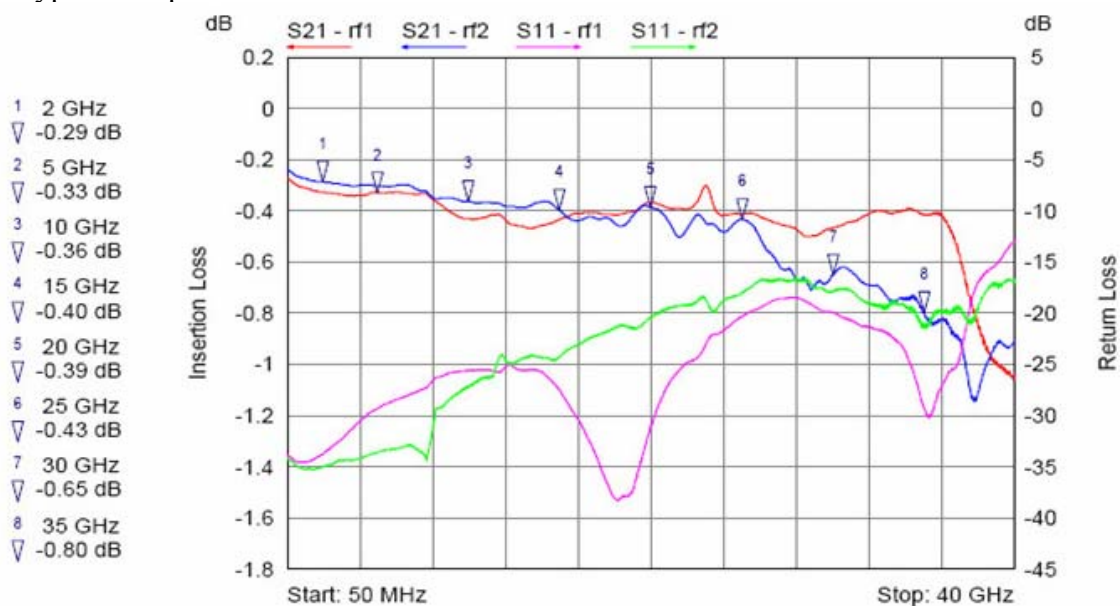


Figure 8: Typical RF performance of a SPDT switch. Source: [www.radantmems.com](http://www.radantmems.com)

As seen in Figure 8, the SPDT RF MEMS features a return loss better than 25 dB from DC to 5 GHz, indicating an excellent match for that frequency, and less than 0.33 dB insertion loss for the same frequency range, which is a very low level of signal attenuation. These measurements suggest that the insertion loss for the entire system (including cables and connectors) will be well under 5 dB. This is a remarkable improvement from the previous switching system which had an insertion loss of about 15 dB at 2.7 GHz.

## 3 Transmission Line Characterization

### 3.1 Coplanar Waveguide

The first objective was to create a simple two port model in ADS network connected by a conductor backed coplanar waveguide transmission line with characteristic impedance of  $50\ \Omega$ . The dielectric material that was used was the FR-4 substrate ( $\epsilon_r=4.4$ , loss tangent = 0.001) with a thickness of 1.5875 mm (62.5 mils). For the copper we were to assume standard 1 oz thickness (1.4 mils). From these parameters the physical dimensions of the coplanar waveguide were determined at 2.7 GHz:  $G=20.5$  mils,  $W=78.18$  mils and  $L=590$  mils.

The circuit was simulated in Momentum. The simulation process combines the Green's functions that were calculated for the substrate of a circuit, plus mesh information that was calculated for the circuit and solves for the currents in the circuit. Using these current calculations, S-parameters are then calculated for the circuit [14]. Adaptive Frequency Sampling (AFS) method was used for the simulations. This method compares sampled S-parameter data points to a rational fitting model.

Figure 9 shows the simulation results,  $S_{11}$  and  $S_{21}$ , for the designed CPW. The return was -22 dB at our operating frequency, 2.7 GHz, indicating a good impedance match between the transmission line and the  $50\ \Omega$  terminations. The insertion loss was less than 0.1 dB at the same frequency, an indication that the amount signal attenuation in the transmission line was negligible.

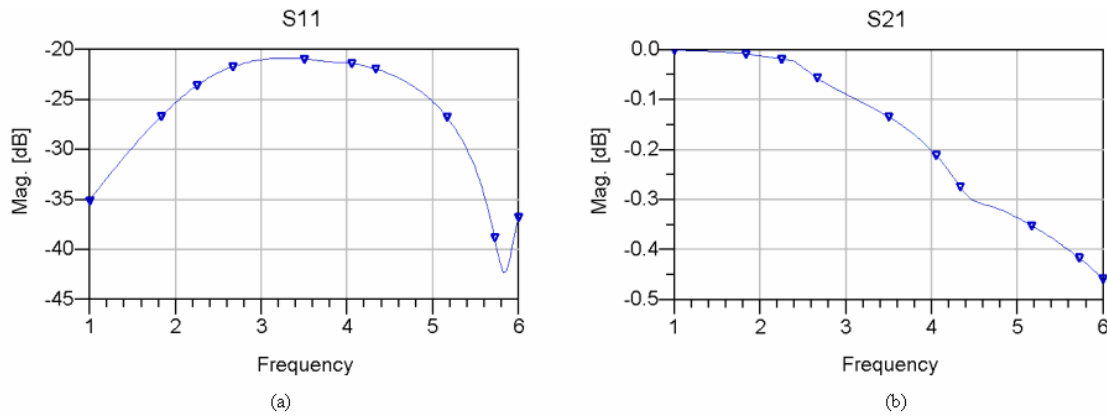
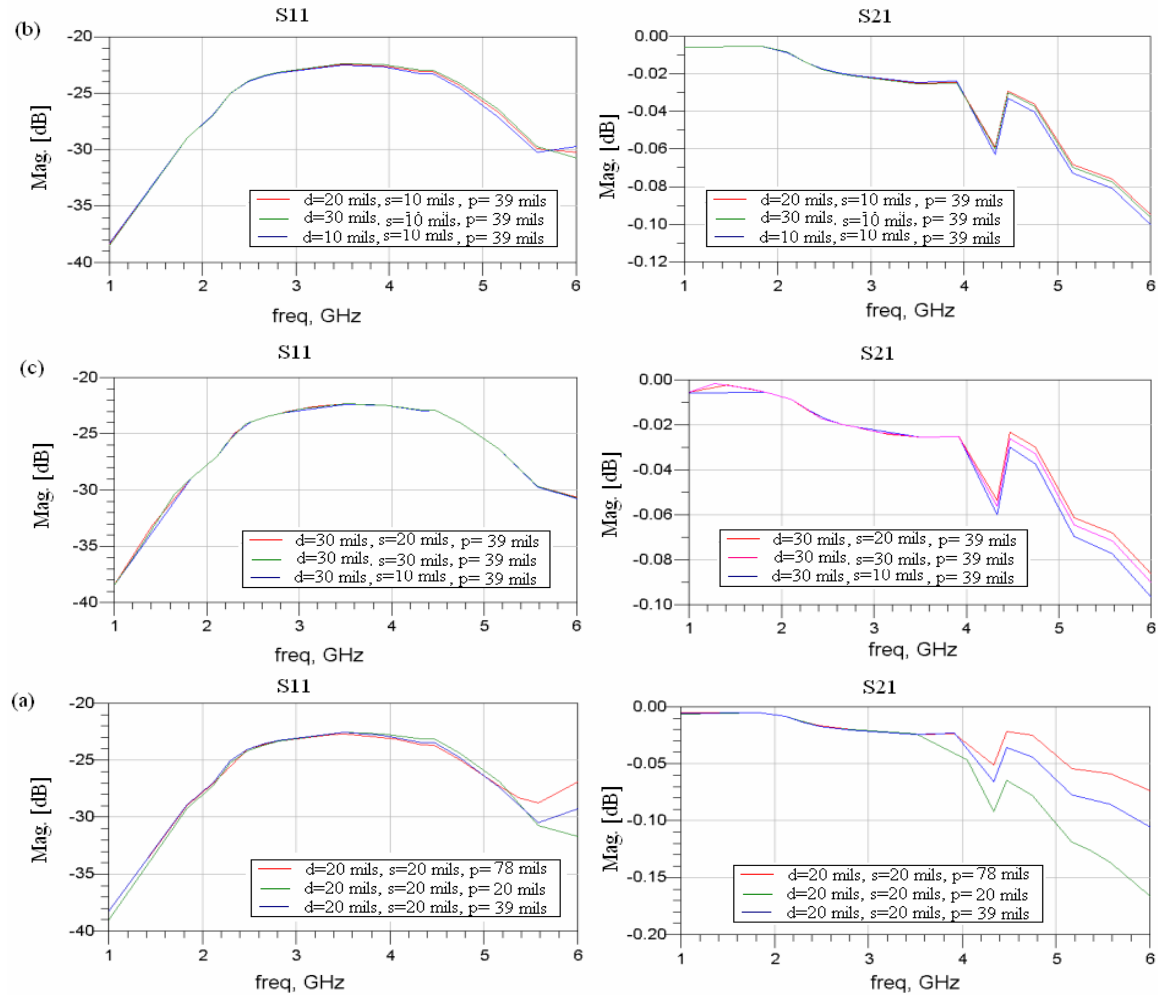


Figure 9: RF performance of  $50\ \Omega$  CPW with  $50\ \Omega$  terminations (a) Return loss (b) Insertion loss

#### 3.1.1 Via Holes

The effect of adding via holes to the CPW on the return loss and insertion loss results was investigated (effect on impedance matching). The following parameters were varied: via hole diameter ( $d$ ), edge to edge separation of the vias ( $s$ ), and the distance of

the vias from slots/gaps on the CPW ( $p$ ). Our nominal design had the following dimensions:  $d=20$  mils,  $s=20$  mils,  $p=39$  mils. The value of the diameter, 20 mils, was chosen because it is a standard drilling size for via holes. The minimum edge to edge separation of via holes requirement is 10 mils [15]. The simulation results for different values of  $d$ ,  $s$  and  $p$  are shown in Figure 10. Comparing the results in Figures 9 and 10, it can be seen that adding via holes improves the insertion loss in the range 1 - 6 GHz. The return loss does not change much in the same frequency range. From Figure 10 it can be seen that the results for the different parameter values shown that there is no significant difference in both the return loss and the insertion at our operating frequency, 2.7 GHz. Hence the choice of the values used in the final design depends on cost of adding the vias: the more via holes per unit area the more expensive it is to fabricate the design. For this design we chose the following parameter values:  $d = 20$  mils,  $s = 30$  mils and  $p = 39$  mils.



**Figure 10: Simulation showing the effect of changing the dimensions and separation of vias (a) Effect of changing the distance of the vias from the slotline (b) Effect of changing the via hole diameter (c) Effect of changing edge to edge separation of the via holes.**

### 3.1.2 Tapering Coplanar Waveguide

The dimensions of the terminal pads on the RF MEMS switches to which the interconnection lines are connected are in the order of microns while the dimensions of the CPW lines are in the order of millimeters. Hence, the lines have to be tapered at the end connecting to the switches. One way this can be done in ADS is shown in Figure 11. The metallization layer (shown in red in the layout below) was defined as the slot layer; objects drawn on the slot layer are opposite of metals, hence they are nonconductive, but the rest of the layer surrounding the objects (shown in black) is conductive. Coplanar mode slot ports with terminal impedances of  $50\Omega$  were included in the layout.

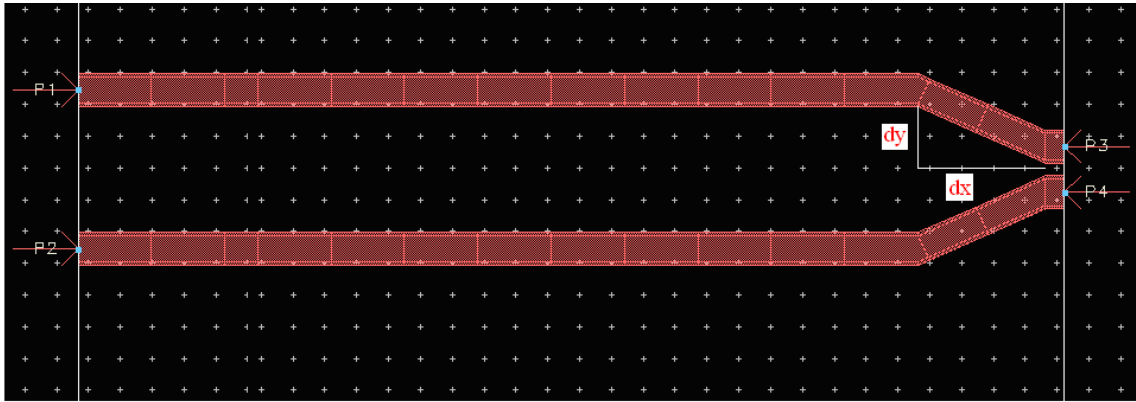


Figure 11: CPW tapering design

The tapers were defined using the parameters ( $dy$  and  $dx$ ) shown above. These parameters define the slope ( $dy/dx$ ) of the inclined part of the taper. The effect of changing the slope was investigated and the results are shown in Figure 12. For these simulations the center conductor width,  $w$ , at the tapered end was maintained at  $300\ \mu\text{m}$ . Port 1 refers to the port at the untapered end while Port 2 refers to the ports at the tapered end, and all the ports were  $50\ \Omega$  terminations.

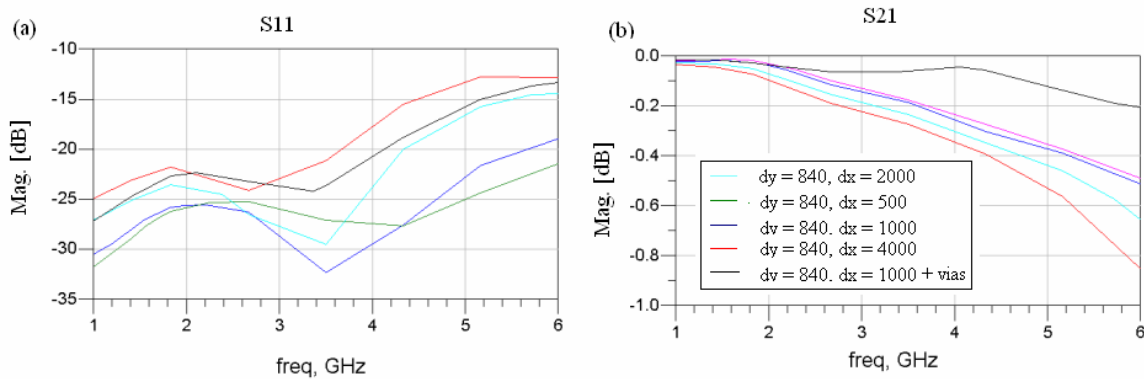


Figure 12: Effects of changing the taper dimensions (a) Return Loss (b) Insertion Loss (all the dimensions are in  $\mu\text{m}$ )

It can be seen from Figure 12 that the parameter values that give the best combination return loss and insertion loss are  $dy = 840 \mu\text{m}$  and  $dx = 1000 \mu\text{m}$ . It can also be noted that for all the designs at 2.7 GHz the return loss is better than 20dB and the insertion loss is less than 0.2 dB, thus any of these taper designs can be used for our final design of the interconnection lines since we require that the insertion loss be less than 1dB and return loss better than 10 dB for the lines. Via holes,  $d = 20$  mils,  $s = 30$  mils and  $p = 39$  mils, were added to one of the tapered CPW,  $dy = 840 \mu\text{m}$  and  $dx = 1000 \mu\text{m}$ , and simulated to evaluate the combined effect of the two design factors. The results are included in Figure 12 (black line). The via hole improved the insertion loss for frequencies greater than 2GHz.

## 3.2 Microstrip

Like in the case of the coplanar waveguide, the first objective was to create a simple two port model network connected by a microstrip transmission line with characteristic impedance of  $50 \Omega$ . FR-4 substrate was used for the design ( $\epsilon_r = 4.4$ , loss tangent = 0.001) with a thickness of 1.5875 mm (62.5 mils). For the copper we were to assume standard 1 oz thickness (1.4 mils). Using these values the dimensions of the microstrip were found to be the following:  $W = 118$  mils and the length,  $L = 1523$  mils. The simulation results for this design are shown in Figure 13.

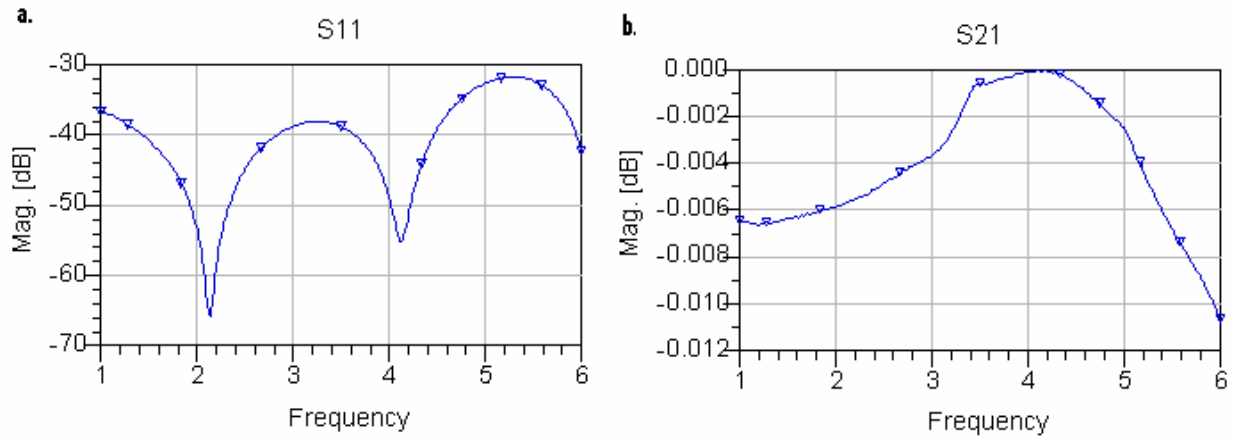
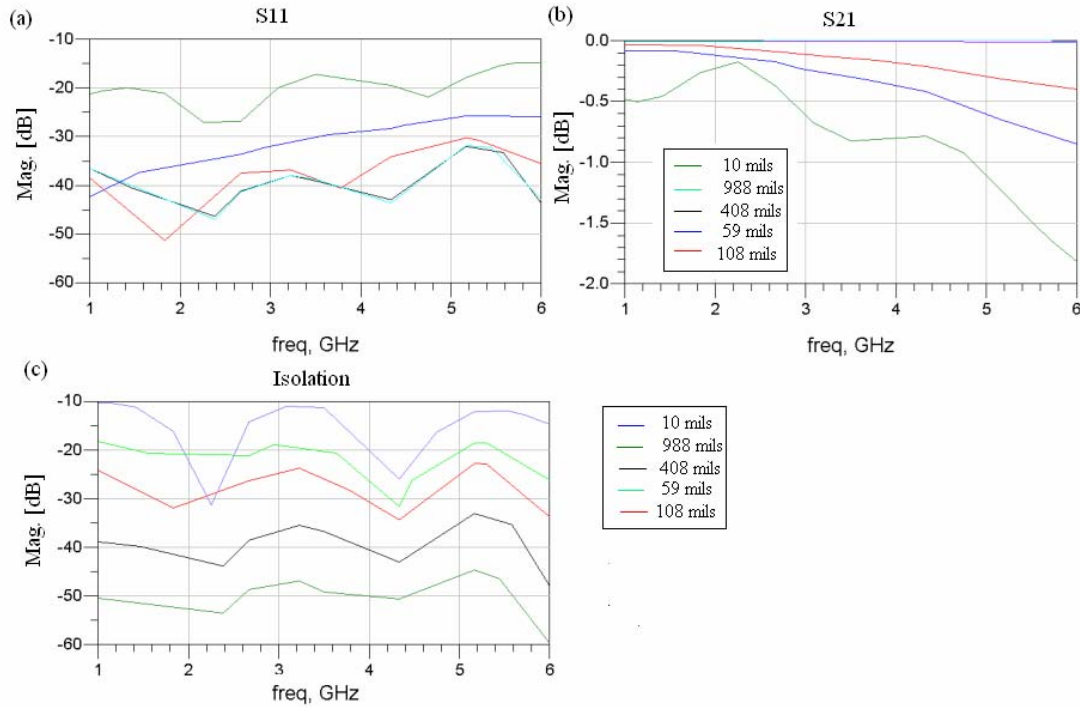


Figure 13: Simulation results of a  $50 \Omega$  microstrip terminated in  $50 \Omega$  ports

### 3.2.1 Coupling

Poor isolation between neighboring lines is one of the main disadvantages of microstrips. Poor isolation worsens the signal to noise ratio (SNR) of the system, and since for active microwave imaging the signals that pass through the lines are very small it is particularly important that the coupling effects of the lines are minimized. This can be achieved by increasing the separation of the lines. However, since the substrate board on which the lines are build has finite dimensions, and several lines are constructed on

the same board, the optimum separation has to be found by setting a minimum value for the isolation. For our design, isolation values equal or greater than 25 dB are sufficient for maintaining a high SNR.



**Figure 14: Effects of varying the separation distance between neighboring lines (a) Return Loss (b) Insertion Loss (c) Isolation**

Figure 14 shows the simulation results for the following separation distances between neighboring lines: 10 mils, 59 mils, 118 mils, 408 mils, and 988 mils.

**Return loss (S11):** For all the separation distances that were used the return loss at 2.7 GHz was better than 20 dB, indicating good impedance matching between the lines and the 50  $\Omega$  terminating ports. Generally, as the separation increases the return loss improves. For separation distances of 108 mils or more the values of the return loss for the coupled lines approach those of a single uncoupled microstrip (see Figure 13 and 14).

**Insertion loss (S21):** The insertion loss also improves with increase in separation distance.

**Isolation:** Isolation increased with increase in separation and this is in agreement with what was expected. For separation distances of 118 mils, 408 mils and 988 mils the isolation was greater than 25 dB. An optimization process was carried out in ADS with the objective of finding the minimum separation that would give a minimum isolation value of 25 dB and the result was found to be around 118 mils. Hence a separation distance of 118 mils can be used for the final design of the switching system.



### 3.2.2 Microstrip Tapering

As was seen in the case of CPW the dimensions of the microstrip transmission like are significantly greater than those of the connecting pads on the MEMS switches. A tapered design that was implemented is shown below. The metallization layer (shown in red in the layout) was defined as a strip conductor layer; objects drawn on this layer are metals. The rest of the layer surrounding the objects (shown in black) is nonconductive.

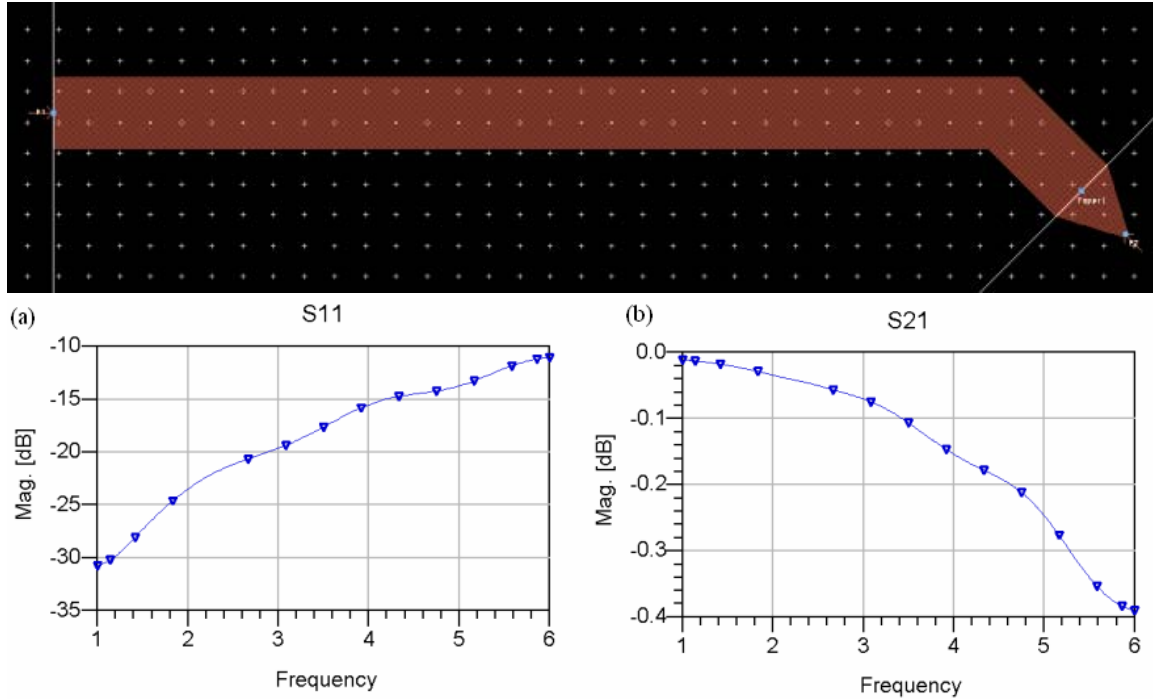


Figure 15: Tapered microstrip design (a) Return loss (b) Insertion loss

The insertion loss was found to be less than 0.1 dB, and the return loss was better than 20 dB at 2.7 GHz. Therefore this design meets our minimum design requirements and can be implemented in the final design.



## 4. Switching System Design

The switching network selects and provides an RF signal path from the vector Network Analyzer (which acts as both the microwave source and receiver) to any combination of Transmit and Receive antennas. The switching system should have the lowest possible insertion loss and provide a good  $50\ \Omega$  impedance match to maximize signal strength, a high level of isolation between channels to minimize crosstalk, and also provide SMA connectivity for easy integration into the system [2]. The proposed switching system uses microelectromechanical system (MEMS) based RF switches that provide a number of improvements over our previous generation of switches. This MEMS based RF switching network will greatly improve the sensitivity of the imaging system and allow for improved spatial sampling density by enabling each antenna to function as both a transmitter and receiver.

### 4.1 Multiplexer Design

The switching system consists of surface mount single-pole double-throw (SPDT) MEMS switches (RMSW220D) and single-pole four-throw (SP4T) MEMS switches (RMSW240).

The switching matrix is comprised of two individual networks: transmitter network and receiver network. Each network consists of four levels; first level with 36 SPDT switches, second level with nine SP4T switches, third level with three SP4T switches and fourth level with a single SP4T. The first level of SPDT switches is common to both networks. Each of the 36 transmitter/receiver antennas is connected to a separate SPDT switch. The SPDT switch determines whether the antenna connected to it is connected to the transmitter network in which case it acts as a transmitting antenna or whether it is connected to the receive network in which case it acts as a receiving antenna. Hence, this matrix system allows the antennas to operate as dual-role transmitter/receivers.

Dual mode operation has the attraction of increasing the amount of measured data since for a given degree of antenna spacing, more transmit and receive points are available. The additional level of SPDT switches also improves the channel to channel isolation of the system. A schematic showing all of the some of the SP4T and SPDT switches for the transmitter network is shown in Figure 16. The receiver network looks exactly the same as the transmitter network except that the fourth level SP4T switch is connected to the detector port of the network analyzer.

Control of the switching network will be performed through a standard parallel port on a PC. For each source-drain connection of the MEMS switch there is a gate which controls whether the signal path is on or off. Hence each SPDT switch has 2 gates and each SP4T switch has four gates. Each of the gates is controlled independently by the power source. A signal path is on if the gate is connected to  $\pm 100\text{V}$  and is off if the gate is connected to  $0\text{V}$ . A signal from the PC will need to be amplified to  $100\text{V}$  in order to turn a switch on.

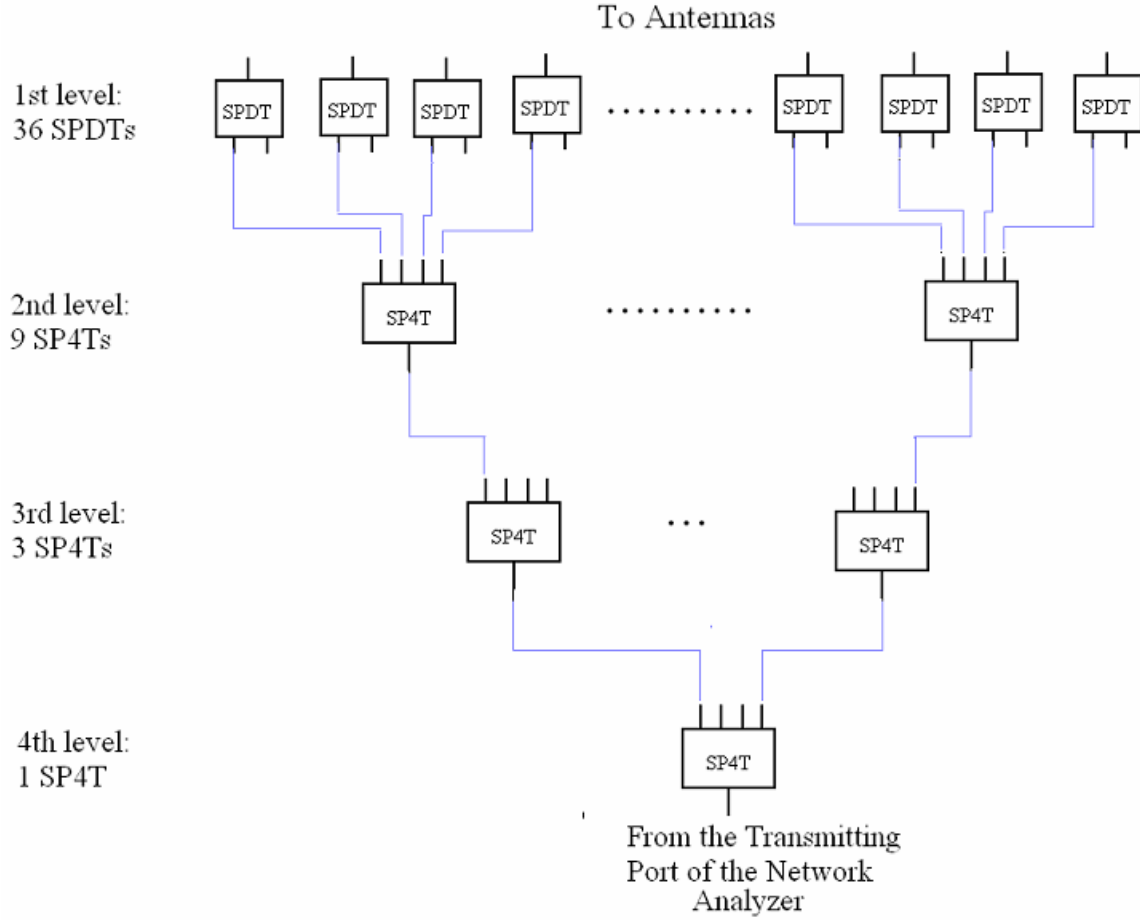


Figure 16: Transmitter switching network. For simplicity only 8 of the 36 total SPDT switches connected to antennas in the imaging chamber are shown.

## 4.2 Switching System Characterization

Characterization of the switching network includes measurements/simulations of insertion loss through the multiplexer tree, and the isolation performance. Insertion loss is a measure of how much of the signal is lost through the system (ideally 0dB), and the isolation characterization is a measure of undesired coupling between channels, which should be made as low as possible [2].

The insertion loss of the current multiplexer was measured to be 15 dB at 2.7 GHz, Figure 17. The simulated insertion loss for the RF MEMS multiplexer is less than 2 dB around the same frequency. We predict that the measured insertion loss after building the multiplexer will not be more than 5 dB, taking into account the coupling effects between connecting lines and impedance mismatches that might be introduced by the fabrication process. This will be a remarkable improvement from the current switching system.

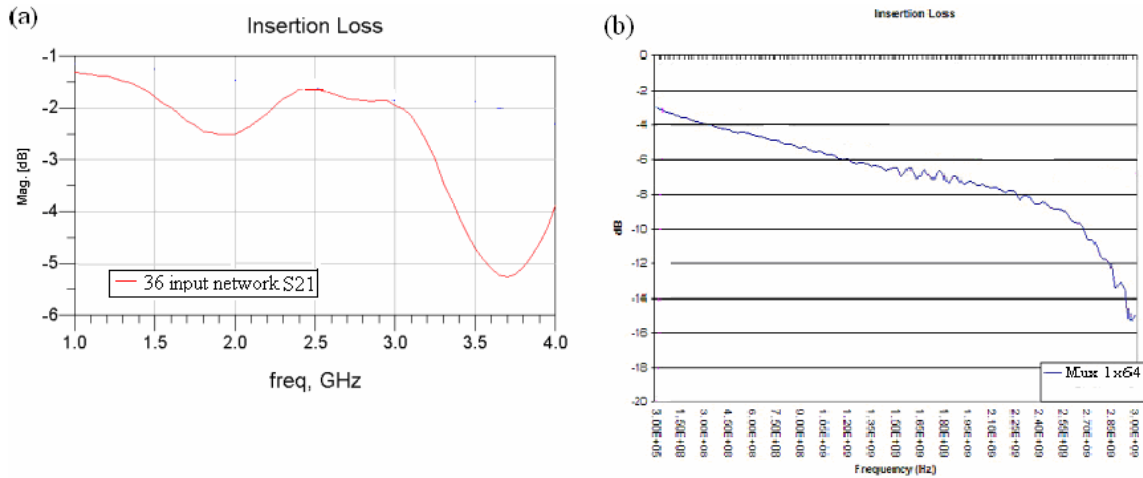


Figure 17: (a) Simulated insertion loss of the new multiplexer (b) Measured insertion loss of the current multiplexer

Figure 18 shows that the selectivity of the current multiplexer switches is around -40dB, which is quite good for this type of multiplexer, but may not be sufficient to ensure that channels carrying strong signals do not obscure the scattering data contained in weaker channels [2]. The simulated value for the RF MEMS multiplexer is around -70dB, which is an improvement from the current switching system.

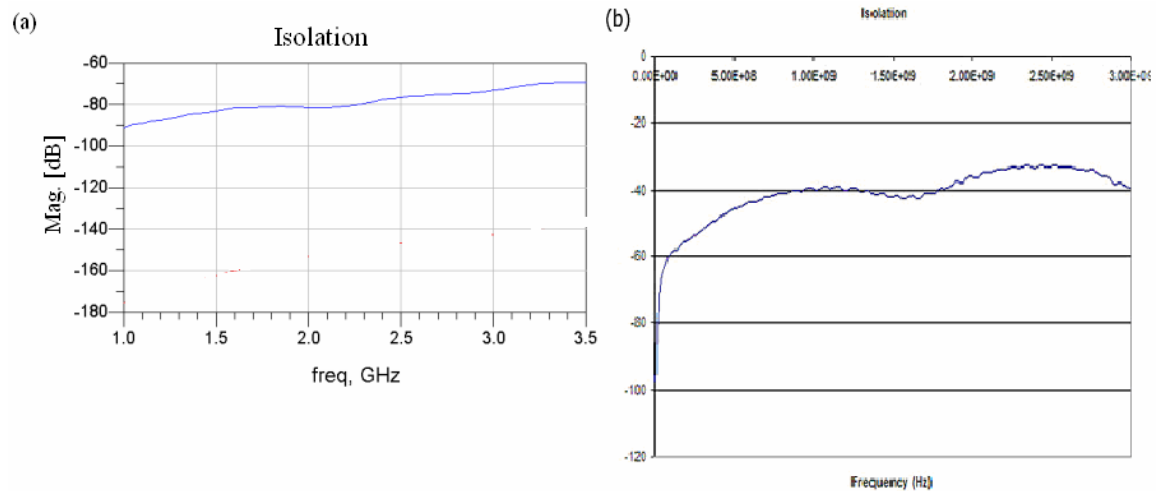


Figure 18: (a) Simulated isolation of the new multiplexer (b) Measured isolation of the current multiplexer

### III. Development of numerical breast phantoms

#### 1. Motivation

Most of the numerical breast phantoms that have been used by the research group at Duke have been limited to relatively simple 3-D phantoms, and have assumed the normal breast tissue to be homogenous. Representative models of human breast which take into account tissue heterogeneity need to be developed. Research on active microwave imaging benefits from anatomically realistic numerical breast models that model structural complexities, tissue heterogeneity, and dispersive dielectric properties [4]. These computational electromagnetics models of microwave interactions with human breast serve as an invaluable tool for improving the design concepts related to microwave breast cancer detection [4].

#### 2. Breast Anatomy

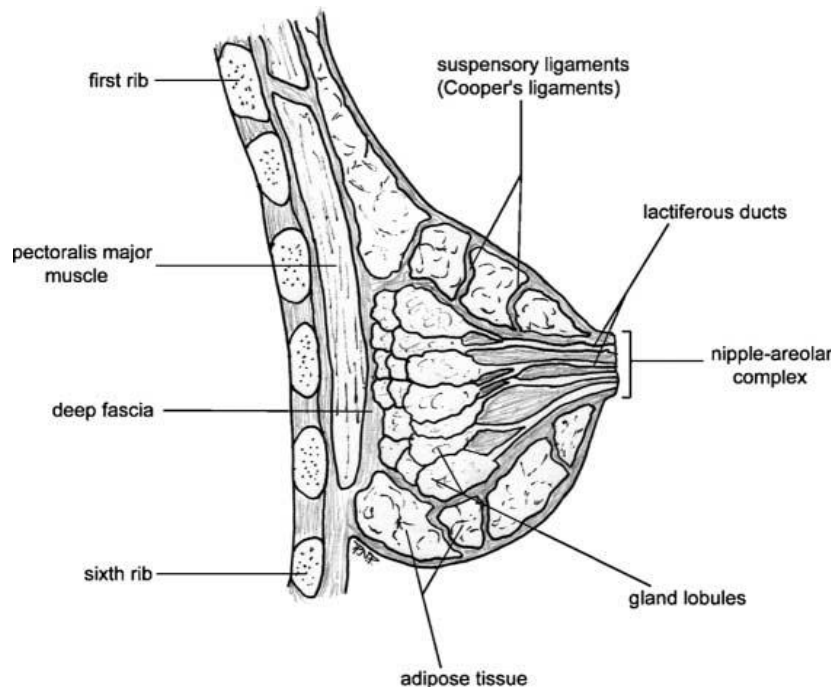


Figure 19: Anatomy of the breast [2]

The adult female breast is a specialized organ which consists of two main tissue types: adipose tissue and glandular tissue [14]. The relative proportions of the two vary widely. They are supported by and attached to the front of the chest wall; they rest on the major chest muscle, the pectoralis major (see Figure 22) [2]. The breast has no muscle tissue and it is supported by semi-elastic bands of tissue referred to as suspensory ligaments (Cooper's ligaments) [2]. In addition, systems of vascular, connective and neural tissues reside among the glandular and fat structures. The key features of each of these elements are described below.

## 2.1 Adipose Tissue

The adipose tissue stores fat in adiposities (lipid-filled cells) and makes up the vast majority of the breast. This tissue can be divided into three main groups: subcutaneous (directly beneath the skin), retromammary (back of the breast), and intraglandular (between the glandular structures) [2]. The subcutaneous and retromammary fat regions form a layer between the majority of the glandular tissue and the external boundaries (skin and pectoralis muscle) of the breast. The majority of cancers develop in the region of glandular tissue within 1 cm of these fat layers. Unfortunately, the layers of fat do not completely isolate the glandular tissue from either the surrounding skin or muscle, which enables the cancer to spread. [2]

## 2.2 Glandular Tissue

The glandular tissue consists of a network of lobules and branching epithelial ducts, which allow for milk production and transport [14]. There are approximately 15-20 lobes in each breast, and each lobe is thought to be exclusively drained by its own individual duct system [2].

## 2.3 Skin and Connective Tissue

The skin acts as the external boundary of the breast. It generally varies in thickness between 0.8mm and 3mm, and skin thickness tends to be inversely proportional to the breast size [2]. The breast is supported by surrounding layer of fascia (connective tissue), which is interspersed with the subcutaneous and retromammary adipose tissue, and by a number of Cooper's ligaments. The connective tissues are often referred to as the breast stroma [14].

# 3. Electrical Properties of Breast Tissue

The contrast that exists between the material properties of healthy and malignant tissue is the fundamental bases of any breast imaging technique [2]. Microwave breast cancer detection has been driven by reports of substantial contrast in the dielectric properties of malignant and normal breast tissues. The contrast has been well documented in a variety of studies [3, 14, 15, 16].

Figure 20 shows the conductivity and permittivity of normal and malignant tissue over the microwave frequency range [2]. There is a variation in the values that has been reported by different research groups; however all the studies show substantial contrast. A statistically rigorous wideband, 0.5-20 GHz, characterization of different breast tissues that was conducted by the Universities of Wisconsin and Calgary showed that microwave imaging is possible at many frequencies; the choice of frequency is largely a matter of balancing the added spatial resolution afforded by higher frequencies with the additional attenuation that comes with it [3].

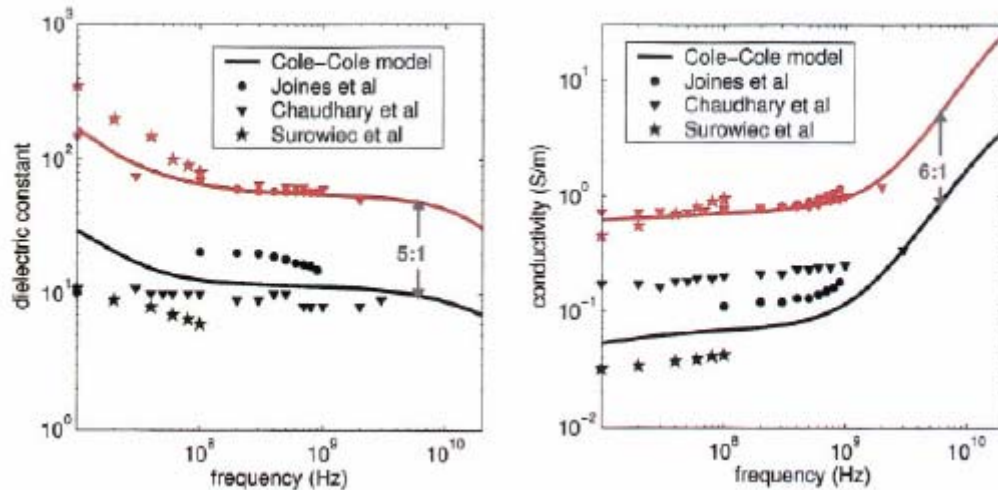


Figure 20: Measured Contrast from Several Studies. Black: Normal, Red: Malignant. [2]

In the development of anatomically realistic 3-D numerical breast phantoms the differences in the electrical properties of different tissue types has to be taken into account. A presentation of the electrical properties of normal breast tissue and malignant tissue is presented below.

### 3.1 Normal Breast Tissue

The physiological heterogeneity in normal breast tissue can be accounted for by dividing the tissue types into three categories: adipose, glandular and fibroconnective tissue [4]. The characterization of normal breast tissue is important because it establishes baseline electrical properties with which the properties of benign and/or malignant tissue can be compared. The effectiveness of microwave breast cancer screening techniques will depend, in part, on the electrical properties of normal tissue [3].

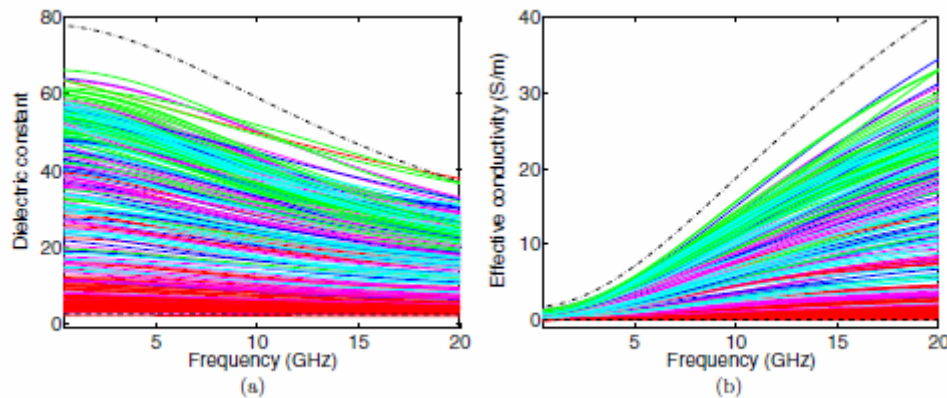
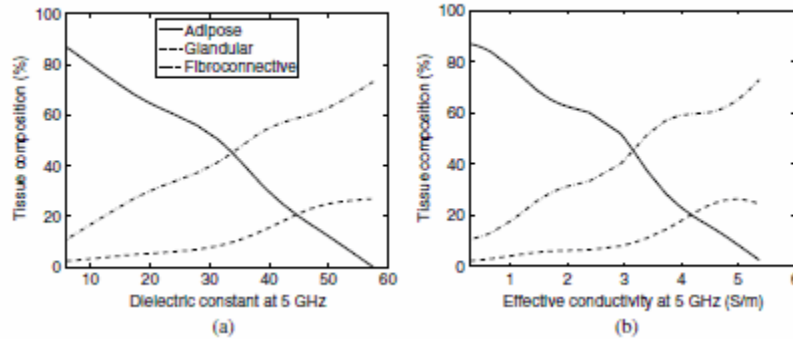


Figure 21: (a) Dielectric constant (b) Effective conductivity. [3]

Figure 21 shows the results of the electrical properties of normal breast tissue from the recently completed large-scale experimental study of normal breast tissue dielectric properties conducted by the Universities of Wisconsin and Calgary [3]. The dashed (lower) black curve corresponds to the dielectric properties of lipid, and the dash-dot (upper) black curve corresponds to the dielectric properties of physiological saline [3].

From the graphs it can be seen that the dielectric properties of normal breast tissue span a large range. At the low end, the tissue dielectric properties are bounded by properties of lipid, and at the high end, the dielectric properties are bounded by the properties of physiological saline. These observed differences are mainly because of the differences in the water content of different normal breast tissue. Water content varies from extremely low (pure adipose) to high (glandular and fibroconnective) [3]. Tissues with higher water content (green curves) have higher values of dielectric constant and effective conductivity, while tissues with lower water content (red curves) have lower dielectric properties. The same results are summarized in Figure 22.



**Figure 22: Percent tissue type as a function of (a) dielectric constant at 5 GHz and (b) effective conductivity at 5 GHz. [3]**

In general as the dielectric constant and effective conductivity of the tissue samples increase, the adipose content decreases and the fibroconnective and/or glandular contents increase [3]. In other words, the dielectric properties of normal breast tissue are primarily determined by the adipose content of the tissue. The results shown in Figure 22 were obtained at 5 GHz, the same trend can be observed at other microwave frequencies.

### 3.2 Malignant Tissue

The adipose and glandular tissue contents of malignant tissue are generally low (0-20% adipose tissue and 10% or less glandular tissue) [14]. The results of the electrical properties of malignant breast tissue from a recent study conducted by the Universities of Wisconsin and Calgary are shown in Figure 23. In general the dielectric properties of malignant tissue are high and span a relatively small range [14]. The majority of the curves are found towards the higher end of the dielectric-properties range. Again, the dashed (lower) black curve corresponds to the dielectric properties of lipid, and the dash-dot (upper) black curve corresponds to the dielectric properties of physiological saline [14].

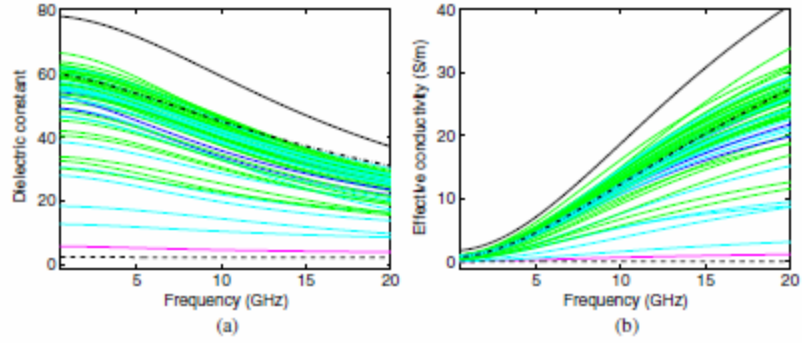


Figure 23: (a) Dielectric constant (b) Effective conductivity. [14]

In general, as the dielectric constant and effective conductivity at 5 GHz increase, the malignant tissue content increases, while the adipose tissue decreases [14]. The same trend can be observed at other microwave frequencies.

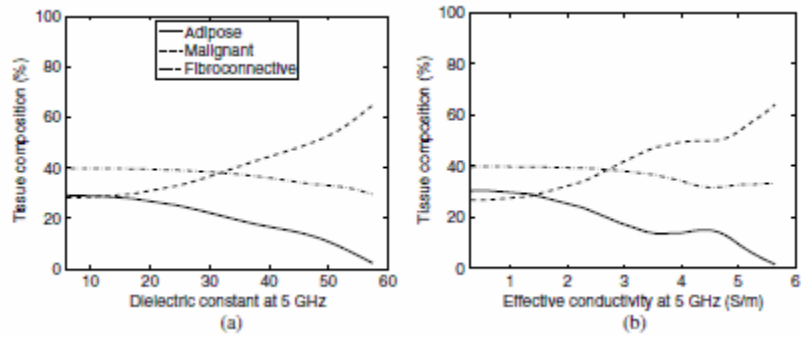


Figure 24: Percent tissue type as a function of (a) dielectric constant (b) effective conductivity at 5 GHz [14]

### 3.3 The relationship of permittivity and conductivity

The relationship between conductivity,  $\sigma$ , and relative permittivity,  $\epsilon'$ , can be parametrized using Debye relaxation equations at any particular microwave frequency in all tissues of a given type [17].

$$\epsilon' = \epsilon_{\infty} + (\epsilon_s - \epsilon_{\infty}) / (1 + \omega^2 \tau^2) \quad \sigma = \epsilon_0 (\epsilon_s - \epsilon_{\infty}) \omega^2 \tau / (1 + \omega^2 \tau^2)$$

where  $\epsilon_s$  and  $\epsilon_{\infty}$  are the low and high frequency limits of the dielectric constant respectively,  $\epsilon_0$  is the permittivity of free space,  $\omega$  is the angular frequency of the applied field and  $\tau$  is the relaxation time.

Assuming that there is only one strongly dominant process occurring at a particular frequency in all tissues of a similar type, then the relationship between the permittivity and conductivity of the tissue at that frequency may be parametrized using the equation above, such that

$$(\sigma - \sigma_s) / (\epsilon' - \epsilon_{\infty}) = \omega^2 \epsilon_0 \tau$$



Therefore for a tissue of a similar type at a particular frequency, a graph of conductivity vs. permittivity should yield a straight line with a gradient  $\omega^2 \epsilon_0 \tau$  [17].

### 3.4 Cole-Cole Models

Cole-Cole models are commonly used to represent wideband frequency-dependent dielectric properties [3]. A single pole can be used to fit breast tissue dielectric properties the microwave frequency range [3]. The equation for a one-pole Cole-Cole model is shown below [3]

$$\epsilon^*(\omega) = \epsilon'(\omega) - j\epsilon''(\omega) = \epsilon_\infty + \frac{\Delta\epsilon}{1 + (j\omega\tau)^{1-\alpha}} + \frac{\sigma_s}{j\omega\epsilon_0}$$

where  $\omega$  is the angular frequency,  $\epsilon'(\omega)$  is the frequency-dependent dielectric constant,  $\epsilon''(\omega)$  is the frequency dependent dielectric loss (which can be converted into effective conductivity,  $\sigma_{eff}(\omega) = \omega\epsilon_0\epsilon''(\omega)$ ), and  $\epsilon_\infty$ ,  $\Delta\epsilon$ ,  $\sigma_s$ ,  $\tau$  and  $\alpha$  are the Cole-Cole model parameters which are estimated from measured data of complex-permittivity,  $\epsilon^*$  [3].

Using the Cole-Cole model the dielectric properties of breast can be compactly represented in terms of the parameters:  $\epsilon_\infty$ ,  $\Delta\epsilon$ ,  $\sigma_s$ ,  $\tau$  and  $\alpha$ . The Cole-Cole representations of wideband dielectric properties can serve as a benchmark in the design of numerical breast phantoms [3].

## IV. Remaining Work and Conclusions

The simulation results of the switching system show that the switching system can be improved by using RF MEMS switches in place of transistor-based electronic switches. The simulation showed that the expected value of the insertion loss of the proposed system at our operating frequency, 2.7 GHz, would be less than 2dB which is a remarkable improvement from the current value of 15 dB for the current system at the same frequency. What remains is to build the multiplexer using the MEMS switches, and measure the S-parameter data. It is expected, however, that the measured value of the insertion loss of the proposed system would be a bit worse than the simulation value of 2 dB but not greater than 5dB. This is because the simulation of the switching system was done in the schematic environment of ADS and this does not take into account the coupling effects between interconnection lines.

The results of the literature study of the dielectric properties of breast tissue show that there is significant contrast in electrical properties of normal breast tissue and malignant tissue. What remains is to use the data collected from the several research groups to develop the anatomically realistic breast phantoms. Structural realism can be achieved through the use of 3-D breast MRIs. The method for mapping breast MRI voxel intensity to accurate dielectric properties normal breast tissue was developed by the research group at the University of Wisconsin [4].

## **Acknowledgements**

I would like express my gratitude to Dr. Ybarra, Dr. Joines, Dr. Liu and Dr. George for the guidance and feedback I received from them throughout my research. I would also like to thank John Stang and Mengqing Yuan for all the help and inspiration they provided throughout my work.

## References:

- [1] P. M. Meaney, M. W. Fanning, D. Li, P. Poplack, D. Paulsen. "A Clinical Prototype for Active Microwave Imaging of Breast," Transactions on Microwave Theory and Techniques, Vol. 48, NO.11, November 2000
- [2] J. P. Stang, "Development of a 3D Active Microwave Imaging System for Breast Cancer Screening," pp. 46-49, 2008
- [3] M. Lazebnik, L. McCartney, D. Popovic, C. B. Watkins, M. J. Lindstrom, J. Harter, S. Sewall, A. Magliocco, J. H. Booske, M. Okoniewski, S. C. Hagness. "A large-scale study of ultrawideband microwave dielectric properties of normal breast tissues obtained from reduction surgeries," Phys. Med. Biol. 52 (2007) 2637-2656
- [4] E. Zastrow, S. K. Davis, M. Lazebnik, F. Kelcz, B. D. Van Veen, S. C. Hagness. "Development of Anatomically Realistic Numerical Breast Phantoms With Accurate Dielectric Properties for Modeling Microwave Interactions With the Human Breast," Vol. 55, pp. 2792-2800, December 2008
- [5] RadantMEMS. Application Note for Test & Handling of SPST RF-MEMS Switches (2009). 4 Apr. 2009  
<[http://www.radantmems.com/radantmems.data/Library/App\\_notes\\_1.4.pdf](http://www.radantmems.com/radantmems.data/Library/App_notes_1.4.pdf)>
- [6] Electromagnetic & Microwave Engineering, em:talk. ADS Tutorial (2009). 5 Apr. 2009 < [http://www.emtalk.com/ads\\_tut\\_1.htm](http://www.emtalk.com/ads_tut_1.htm)>
- [7] Electromagnetic & Microwave Engineering, em:talk. ADS Tutorial (2009). 5 Apr. 2009 < [http://www.emtalk.com/ads\\_tut\\_1.htm](http://www.emtalk.com/ads_tut_1.htm)>
- [8] P-N Designs, Inc. Coplanar Waveguide. 4 Mar. 2006. 7 Apr. 2009  
<http://www.micowaves101.com/encyclopedia/coplanarwaveguide.cfm#types>
- [9] Computer Simulation Technology, CST. Conductor Backed Coplanar Waveguide (2009). 7 Apr. 2009  
<http://www.cst.com/Content/Applications/Article/Conductor+Backed+Coplanar+Wave+Guide>
- [10] N. I. Dib, L. P. B. Katchi. "Theoretical Characterization of Coplanar Waveguide Lines and Discontinuities," pp. 1-9, November 1992
- [11] W. T. Joines. "Elements of Electromagnetic Communications," Duke University, pp 50-51, 2007
- [12] K. W. Whites. "Microstrip. ADS and LineCalc," pp. 1-18, 2005
- [13] S. H. Zainud-Deen, W. M. Hassen, E. M. Ali, K. H. Awadalla, H. A. Sharshar. "Breast Cancer Detection using a Hybrid Finite Difference Frequency Domain and

Particle Swarm Optimization Techniques,” Progress In Electromagnetics Research B, Vol. 3, 35-46, 2008

[14] M. Lazebnik, D. Popovic, L. McCartney, C. B. Watkins, M. J. Lindstrom, J. Harter, S. Sewall, T. Ogilvie, A. Magliocco, T. M. Breslin, W. Temple, D. Mew, J. H. Booske, M. Okoniewski, S. C. Hagness. “A large-scale study of ultrawideband microwave dielectric properties of normal, benign and malignant breast tissues obtained from cancer surgeries,” *Phys. Med. Biol.* 52 (2007) 6093-6115

[15] W. T. Joines, Y. Zhang, C. Li, R. L. Jirtle. “The measured electrical properties of normal and malignant human tissues from 50 to 900 MHz,” *Med. Phys.* 21(4), April 1994

[16] J. Andrzej, S. S. Stuchly, J. R. Barr, A. Swarup. “Dielectric Properties of Breast Carcinoma and the Surrounding Tissues,” *Transactions of Biomedical engineering*, Vol. 35, NO. 4, April 1988

[17] A. M. Campbell, D. V. Land. “Dielectric Properties of Female Human Breast Tissue measured in vitro at 3.2 GHz,” *Phys. Med. Biol.*, 1992, Vol. 37, No 1, 193-210